Published in

Appl. Phys. Lett. **103**, 054104 (2013)

http://link.aip.org/link/doi/10.1063/1.4817257

Spectroscopic imaging of self-organization in high power impulse magnetron sputtering plasmas

Joakim Andersson,[a,b] Pavel Ni,[a] and André Anders[a,*]

[a)] Lawrence Berkeley National Laboratory, 1 Cyclotron Road, Berkeley, California 94720, USA

[b)] Centre for Quantum Technologies, National University of Singapore, 3 Science Drive 2, 117543 Singapore, Singapore

[*)] Author to whom correspondence should be addressed. Electronic mail: aanders@lbl.gov

revised version of 2013-07-16

Excitation and ionization conditions in traveling ionization zones of high power impulse magnetron sputtering plasmas were investigated using fast camera imaging through interference filters. The images, taken in end-on and side on views using light of selected gas and target atom and ion spectral lines, suggest that ionization zones are regions of enhanced densities of electrons, and excited atoms and ions. Excited atoms and ions of the target material (Al) are strongly concentrated near the target surface. Images from the highest excitation energies exhibit the most localized regions, suggesting localized Ohmic heating consistent with double layer formation.

ACKNOWLEDGMENT

The authors thank the LBNL Fusion Group for lending the fast camera and providing support to P.N. J.A. acknowledges support from the National Research Foundation and the Ministry of Education, Singapore. This work was supported by the Assistant Secretary for Energy Efficiency and Renewable Energy, Office of Building Technology, of the U.S. Department of Energy under Contract No. DE-AC02-05CH11231.

DISCLAIMER

This document was prepared as an account of work sponsored by the United States Government. While this document is believed to contain correct information, neither the United States Government nor any agency thereof, nor The Regents of the University of California, nor any of their employees, makes any warranty, express or implied, or assumes any legal responsibility for the accuracy, completeness, or usefulness of any information, apparatus, product, or process disclosed, or represents that its use would not infringe privately owned rights. Reference herein to any specific commercial product, process, or service by its trade name, trademark, manufacturer, or otherwise, does not necessarily constitute or imply its endorsement, recommendation, or favoring by the United States Government or any agency thereof, or The Regents of the University of California. The views and opinions of authors expressed herein do not necessarily state or reflect those of the United States Government or any agency thereof or The Regents of the University of California.

When energy is supplied from external sources to an open system, entropy is reduced and dissipative structures can evolve. This is exemplified by often beautiful patterns in all kinds of biological, chemical and physical systems.[1] Plasma systems are no exceptions, and pattern formation is generally associated with waves and instabilities. Various types of instabilities have been identified for $\mathbf{E}\times\mathbf{B}$ devices such as Hall thrusters,[2-6] microwave-generating electron magnetrons,[7] and sputtering magnetrons.[8] Pronounced moving structures have recently been described by several groups when sputtering magnetrons are operated with high power pulses, i.e. in the high power impulse magnetron sputtering (HiPIMS) mode.[9-11] Various suggestions have been made as to the origin of these self-organized, moving structures. While the exact nature of the instability and structure formation is still subject to research, there is agreement that the patterns are associated with enhanced excitation, ionization, and the formation of traveling electric field regions having a component parallel to the target surface.[9-12]

In this contribution we use high speed spectroscopic imaging to elucidate some features of traveling ionization zones. We extend previous work[9-11,13] by combining high temporal resolution (<< 1 μs) with sufficient spectral resolution ($\Delta\lambda$ < 10 nm) to obtain images in spectrally selected light specific to the neutral atoms and singly charged ions of the gas and the target material.

In preparation for spectroscopic imaging, optical emission spectra were studied for HiPIMS discharges using different targets in argon background of typically 0.5 Pa. We concluded that aluminum is a preferred target material in this context because (a) aluminum shows strong atom and ion spectral lines within the sensitivity range of the camera's photodetector (wavelength from about 290 nm to about 810 nm) and (b) those target lines are clearly spectrally separated from the atom and ion lines of argon. Hence, with aluminum one can obtain images using the light of target atoms, target ions, gas atoms, or gas ions, depending on the spectral filter used.

Highly transmitting narrow-band filters were used, whose nominal spectral transmission centers were as follows: 394 nm (Al I), 436 nm (Ar II), 480 nm (Ar II), 630 nm (Al II), 694 nm (Ar I), 810 nm (Ar I). We use here the spectroscopic notation, e.g. Al I is the neutral Al atom, and Al II is the singly charged Al ion. The details of the filter properties and the strong spectral lines in the transmittance band of each filter are given in the supplementary material. An important point is that the images represent very different upper excitation levels, covering the range from 3.14 eV for the 394 nm filter for Al I lines to 19.5 eV for the 436 nm filter for Ar II lines. This implies that the images contain information not only on atom or ion densities but also on the excitation conditions. We will come back to this point when looking at the results.

The experimental details of the discharge system and imaging setup are similar to our previous reports without filters[11,14] and shown in part 1 of the supplementary material.[15] HiPIMS pulses were produced using a commercial pulser (SIPP by Melec GmbH). Most pulses were driven by a voltage of 550 V, with the pulse length and repetition rate set to 50 μs and 100 pulses per second, respectively. The current pulse shape was triangular which indicates that the discharge had not yet reached its steady-state level.[16] This implies that different current levels are imaged when the camera was triggered at different times within the pulse: later times mean higher currents.

The target had a diameter of 76 mm (3 inch) and a thickness of 6.2 mm (1/4 inch). The magnetron was unbalanced. The target was magnetically clamped and the grounded anode ring was flush with the target; these details are important since they allowed us to have an unobstructed side-on view. Two views were recorded: (a) a straight "end-on" view at the target disk, and (b) a glancing angle side-on view.

The images were taken with a Princeton Instruments "PI-MAX 1024" camera equipped with a microchannel plate image amplifier. The exposure time was always 150 ns, which was short enough to avoid blurring by the motion of the ionization zone.[11] The intensities are presented in false color using the color scale "royal" of the image processing software ImageJ.[17]

Unfortunately, the camera can only take one image at a time, and therefore the individual images shown in Figs. 1 and 2 are taken from different HiPIMS pulses. While the general character of the images is very similar from pulse to pulse, details like the number, location, and size of ionization zones and plasma flares vary. It would have been desirable to simultaneously take images in different spectral lights from the same emitting plasma.

The recorded brightness is not only a function of the discharge conditions but also depends on the lens aperture, the gain settings of the image amplifier, and the spectral sensitivity of the photon detector. Furthermore, the selection of the false-color look-up table "royal" amplifies the contrast. Therefore, one should be cautious when comparing apparent light intensity and contrast of different images.

The rows are sorted by the upper level of the electronic transition. Aluminum neutrals are standing out because the upper level is only 3.14 eV, with the excitation starting from the ground state. This is in stark contrast to all other transitions, where the upper level is higher than 13 eV. Therefore, neutral aluminum emission is dominated by excitation by low-energy, thermalized electrons, whereas the other transitions are indicative for more energetic electrons, either from the tail of the Maxwellian part of the energy distribution, or from secondary electrons.

As one may have anticipated, images using light from different species and excitation levels have quite different appearances. The top rows of Figs. 1 and 2 contain images taken without spectral filter, i.e. light is integrated over the spectral range of the camera. The next row in each figure shows light from neutral aluminum atoms. In end-on view, Fig. 1 row (b), light emission shows structure and is spatially widely distributed, while in side-on view, Fig. 2 row (b), the emission is practically limited to the region no more than 3 mm from the target. The next row, taken with a filter transmitting light around 810 nm, shows light from neutral argon, which is also widely distributed. In contrast, the light emitted by aluminum ions (630 nm filter) and argon ions (480 nm and 436 nm filters) exhibits strong localization in ionization zones (Fig. 1), and ejection of plasma jets or flares (Fig. 2). The perhaps most important observation is that ionization zones appear much sharper in the light of ions, and especially when considering levels of high excitation energy. This clearly indicates that (a) those zones are the essential regions of concentrated ionization, and (b) the electron energy is locally high, i.e. these zones are regions of energy dissipation.

The total line intensity of light of wavelength λ_{ul} emitted per solid angle from atoms in an optically thin plasma of thickness D is proportional to the number density n_u of atoms excited in the upper energy level E_u and the rate of spontaneous decay from the upper level *u* to the lower level *l*, as described by the Einstein coefficient A_{ul},

$$I_{ul} = \frac{h\nu_{ul}}{4\pi} A_{ul}\, n_u\, D\,, \tag{1}$$

where $h\nu_{ul}$ is the photon energy associated with the wavelength. The density of excited states is generally described by a collisional-radiative model since the local thermal equilibrium model (dense

plasma) or corona model (low density plasma) may not be applicable. Assuming that most atoms are in the ground state of density n_0 , the rate of producing excited atoms can be expressed by

$$\left(\frac{\partial n_u}{\partial t}\right)_{excitation} = K_{0u} n_0 n_e \tag{2}$$

where

$$K_{0u} = \int f_e(\varepsilon)\, \varepsilon^{1/2}\, \sigma_{0u}(\varepsilon)\, d\varepsilon \tag{3}$$

is the rate of excitation, $f_e(\varepsilon)$ is the electron energy distribution function, and $\sigma_{0u}(\varepsilon)$ is the excitation cross section. Those expressions capture the essence to be discussed: the intensity of light from atoms is proportional to the density of atoms, the density of electrons, and determined by the electron energy distribution in relation to the specifics of the atomic properties. Therefore one cannot infer on only the density of atoms or only on the electron temperature in an isolated manner, rather, the images contain a convolution of information.

Considerations for ions are analogous, though ions need to be produced in the first place (first ionization energies for Al and Ar are 5.99 eV and 15.76 eV, respectively). Ionization followed by excitation amplifies the fact that the ionization zones are regions of greatest energy dissipation.

A beautiful illustration of the role of excitation by electron impact is shown in Fig. 2, top row, image taken at 42 µs, 100 A (an enlarged detail of which is available as Supplementary Material). Bright arches must be caused by excitation by magnetized electrons since an arched formation of ground-state neutrals or ions is unreasonable.

In previous work[11,12] it was proposed that ionization zones have increased "stopping power" for high energy electrons because electrons are more likely to interact with atoms, ions, and other electrons when the density of those particles is high. When interacting, energy is transferred from hot electrons, providing a positive feedback to cause even more ionization at that location. However, in very recent work by Hou *et al.*[18] it was shown that heating by secondary electrons is not the dominant mechanism of power dissipation in magnetrons. Rather, plasma electrons are predominantly "energized" by Ohmic heating in the magnetic presheath, where the electron cross-field current density is high *and* the electric potential gradient is still large. Applying this finding to the interpretation of images in Figs. 1 and 2 suggests that power dissipation is concentrated in ionization zones, with a power density of Ohmic heating

$$p_{IZ} = j_{IZ}\, \Delta V_{IZ} / \Delta L \ , \tag{4}$$

where j_{IZ} , ΔV_{IZ} and ΔL are the current density, the voltage drop, and the thickness of an ionization zone. The local current density can be substantially larger than the discharge current density due to closed drift of electrons. Although locally resolved measurements by Lundin and coworkers[19] excluded the interesting region very close to the target one may extrapolate their data and find that the azimuthal current exceeds the discharge current I by one order of magnitude, or more. One can certainly write $j_{IZ} > I / A_{IZ}$, where A_{IZ} is a characteristic cross section area of the ionization zone. From images one can determine $A_{IZ} < 10^{-4}\ \mathrm{m}^2$, leading to $j_{IZ} > 10^6\,\mathrm{A/m}^2$. Probe measurements, formation of plasma flares in *z*-direction, and azimuthally asymmetric particle ejection suggest that each

zone is associated with a traveling double layer, where the layers' potential drop parallel to the target is at least 10 V and the thickness is of order 10^{-3} m. This leads to a high power density of $p_{IZ} > 10^{10}\ \mathrm{W/m^3}$, and likely $p_{IZ} > 10^{11}\ \mathrm{W/m^3}$. Additional local Ohmic heating, of roughly the same order of magnitude, is caused by electrons experiencing a potential drop in the *z*-direction,[18] i.e. when escaping the closed drift and forming plasma flares.[14]

In summary, spectroscopic images of short exposure times showed that (i) emission from metal atoms of low excitation energy appears in more-or-less periodically structured zones spreading broadly across the racetrack, (ii) emission from increasingly higher energy levels, especially from ions, is concentrated in ionization zones, (iii) emission from target atoms and ions is primarily from a region less than 3 mm from the target surface, whereas emission from gas atoms and ions is much more distributed, with the greatest emission far from the target region coming from argon ions. The observations are compatible with the concept that each ionization zone has a double layer responsible for plasma flare formation, asymmetric particle emission, and localized Ohmic heating. Ionization zones are driven by an ionization instability; they represent self-organized dissipative structures typical for open systems.

References

[1] H. Haken, *Synergetics: Introduction and Advanced Topics* (Springer, Berlin, 2004).

[2] E. Chesta, C. M. Lam, N. B. Meezan, D. P. Schmidt, and M. A. Cappelli, IEEE Trans. Plasma Sci. **29,** 582 (2001).

[3] E. Choueiri, Phys. Plasmas **8,** 1411 (2001).

[4] C. L. Ellison, Y. Raitses, and N. J. Fisch, Phys. Plasmas **19,** 013503 (2012).

[5] D. Yu, C. Wang, L. Wei, C. Gao, and G. Yu, Phys. Plasmas **15,** 113503 (2008).

[6] E. Fernandez, M. K. Scharfe, C. A. Thomas, N. Gascon, and M. A. Cappelli, Phys. Plasmas **15,** 012102 (2008).

[7] R. C. Davidson, *Introduction to the Physics of Nonneutral Plasmas* (Addison-Wesly, Redwood City, CA, 1990).

[8] S. N. Abolmasov, Plasma Sources Sci. Technol. **21,** 035006 (2012).

[9] A. Kozyrev, N. Sochugov, K. Oskomov, A. Zakharov, and A. Odivanova, Plasma Physics Reports **37,** 621 (2011).

[10] A. P. Ehiasarian, A. Hecimovic, T. de los Arcos, R. New, V. Schulz-von der Gathen, M. Böke, and J. Winter, Appl. Phys. Lett. **100,** 114101 (2012).

[11] A. Anders, P. Ni, and A. Rauch, J. Appl. Phys. **111,** 053304 (2012).

[12] A. Anders, Appl. Phys. Lett. **100,** 224104 (2012).

[13] M. Hála, O. Zabeida, B. Baloukas, J. E. Klemberg-Sapieha, and L. Martinu, IEEE Trans. Plasma Sci. **38,** 3035 (2010).

[14] P. A. Ni, C. Hornschuch, M. Panjan, and A. Anders, Appl. Phys. Lett. **101,** 224102 (2012).

[15] See supplementary material at http://dx.doi.org/10.1063/1.4817257 for the experimental setup, for the wavelength and spectroscopic information on the spectral lines used, and for an enlarged detail of an image taken with spectrally integrated light at 100 A discharge current.

[16] A. Anders, J. Andersson, and A. Ehiasarian, J. Appl. Phys. **102,** 113303 (2007).

[17] W. Rasband, *ImageJ 1.44p, downloaded from http://imagej.nih.gov/ij* (National Institute of Health, 2011).

[18] C. Huo, D. Lundin, M. A. Raadu, A. Anders, J. T. Gudmundsson, and N. Brenning, Plasma Sources Sci. Technol. **22,** 045005 (2013).

[19] D. Lundin, S. A. Sahab, N. Brenning, C. Huo, and U. Helmersson, Plasma Sources Sci. Technol. **20,** 045003 (2011).

Figure Captions

Fig. 1 Compilation of end-on views with parameters as indicated. Each image was taken with 150 ns exposure from a different HiPIMS pulse. Top row: spectrally integrated images with aperture 4.0, and below taken through interference filters and using aperture 2.0. Details of interference filters and the spectroscopic data of the lines are compiled in the Supplementary Material.[15] The feature near the top left corner of some images is a reflection from the window's shutter. The scale shown applies to all images.

Fig. 2 Compilation of side-on views with parameters as indicated. Images in the first column, 22 µs into the pulse, at 25 A, were taken with aperture 2.0, while all the others were taken with aperture 8. The images of the last column are again at 100 A but with falling current, just a couple of microseconds after the voltage pulse was switched off. The scale shown applies to all images. An enlarged detail of the image at 100 A, using spectrally integrated light, is provided in the Supplementary Material.[15]

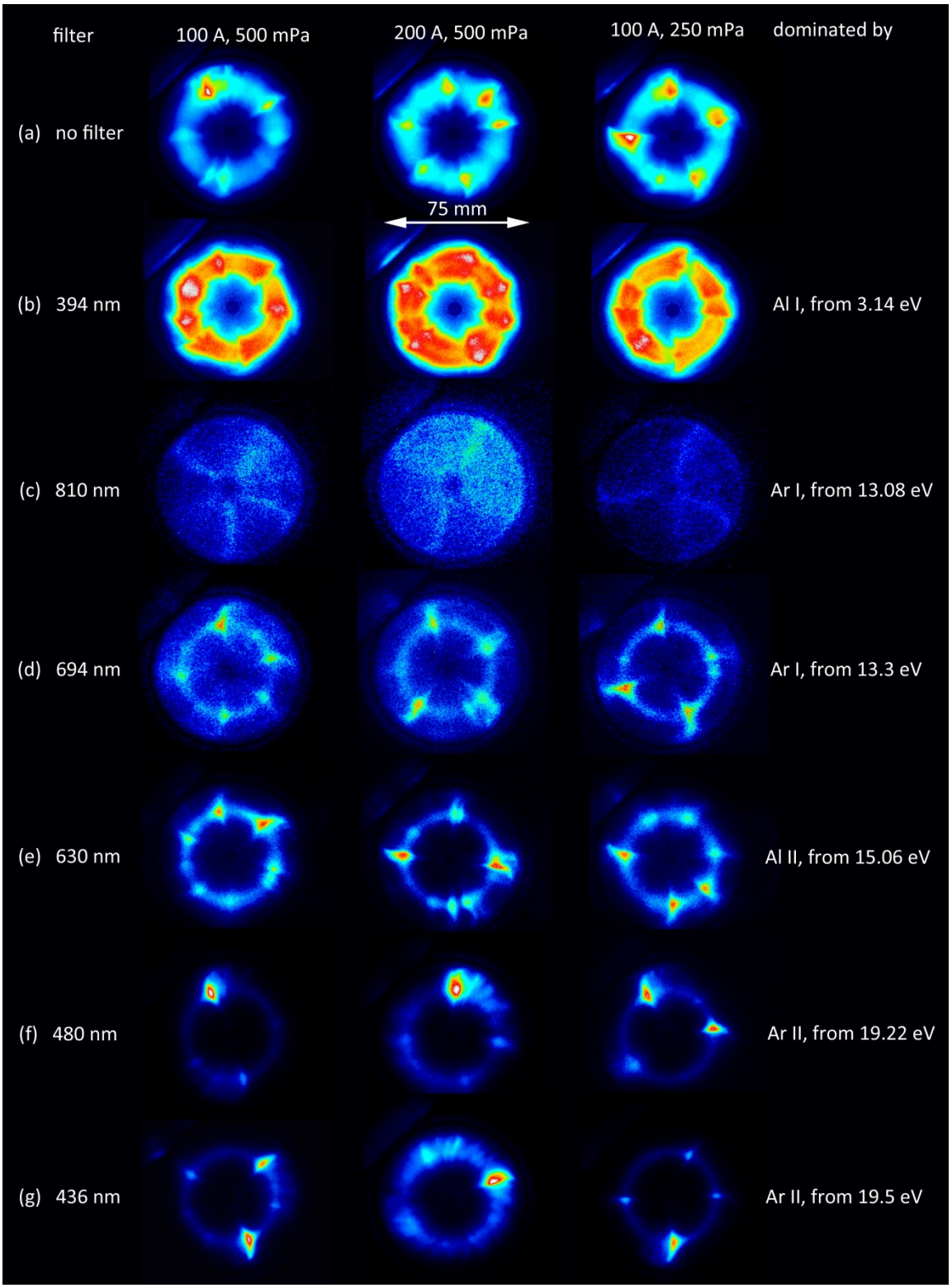
filter
100 A, 500 mPa
200 A, 500 mPa
100 A, 250 mPa
dominated by
(a) no filter
75 mm
(b) 394 nm
Al I, from 3.14 eV
(c) 810 nm
Ar I, from 13.08 eV
(d) 694 nm
Ar I, from 13.3 eV
(e) 630 nm
Al II, from 15.06 eV
(f) 480 nm
Ar II, from 19.22 eV
(g) 436 nm
Ar II, from 19.5 eV

Figure 1

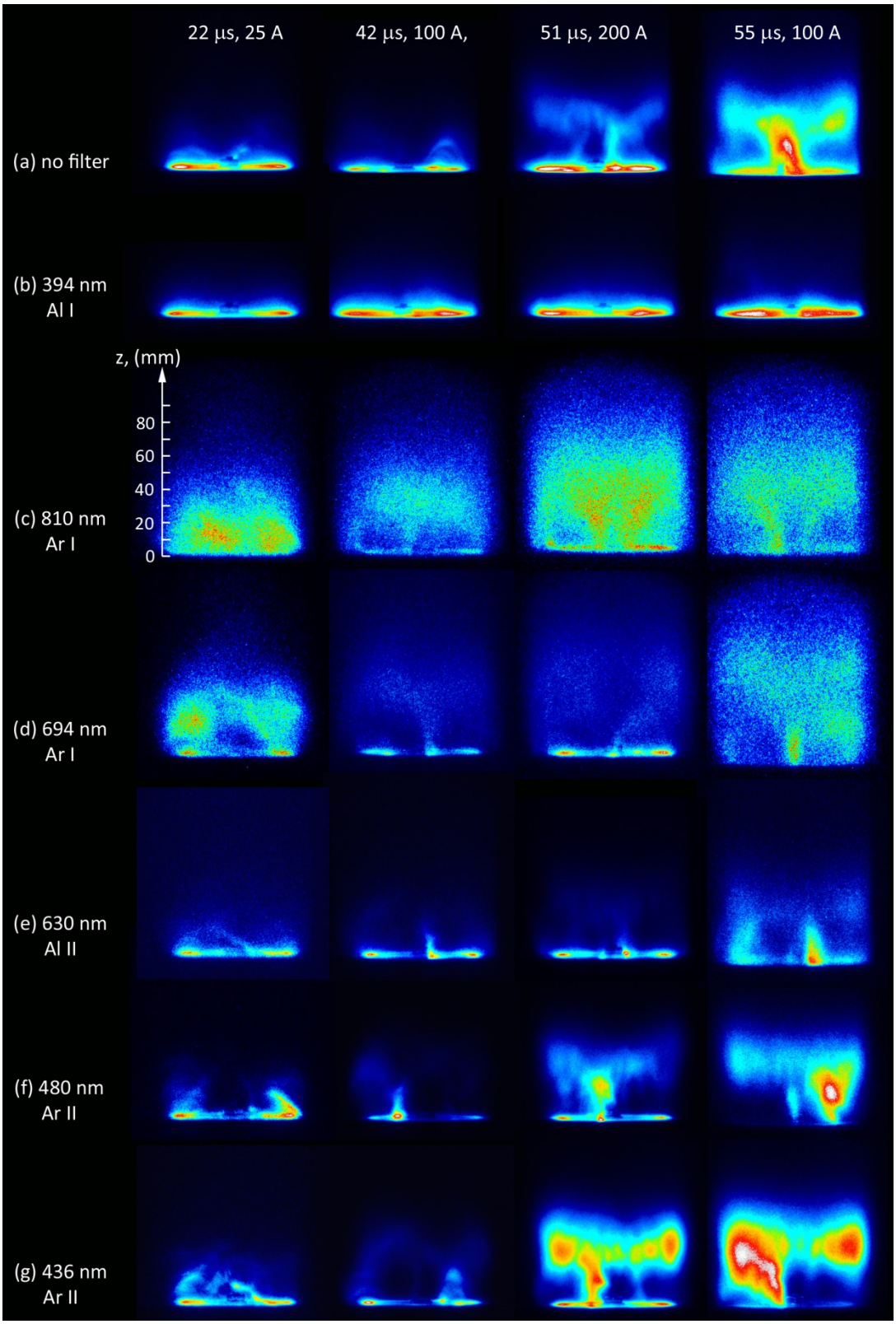
22 µs, 25 A
42 µs, 100 A,
51 µs, 200 A
55 µs, 100 A
(a) no filter
(b) 394 nm
Al I
z, (mm)
80
60
40
20
0
(c) 810 nm
Ar I
(d) 694 nm
Ar I
(e) 630 nm
Al II
(f) 480 nm
Ar II
(g) 436 nm
Ar II

Figure 2

Supplementary material, part 1.

Experimental setup for end-on and side-on imaging of the magnetron working in HiPIMS mode.

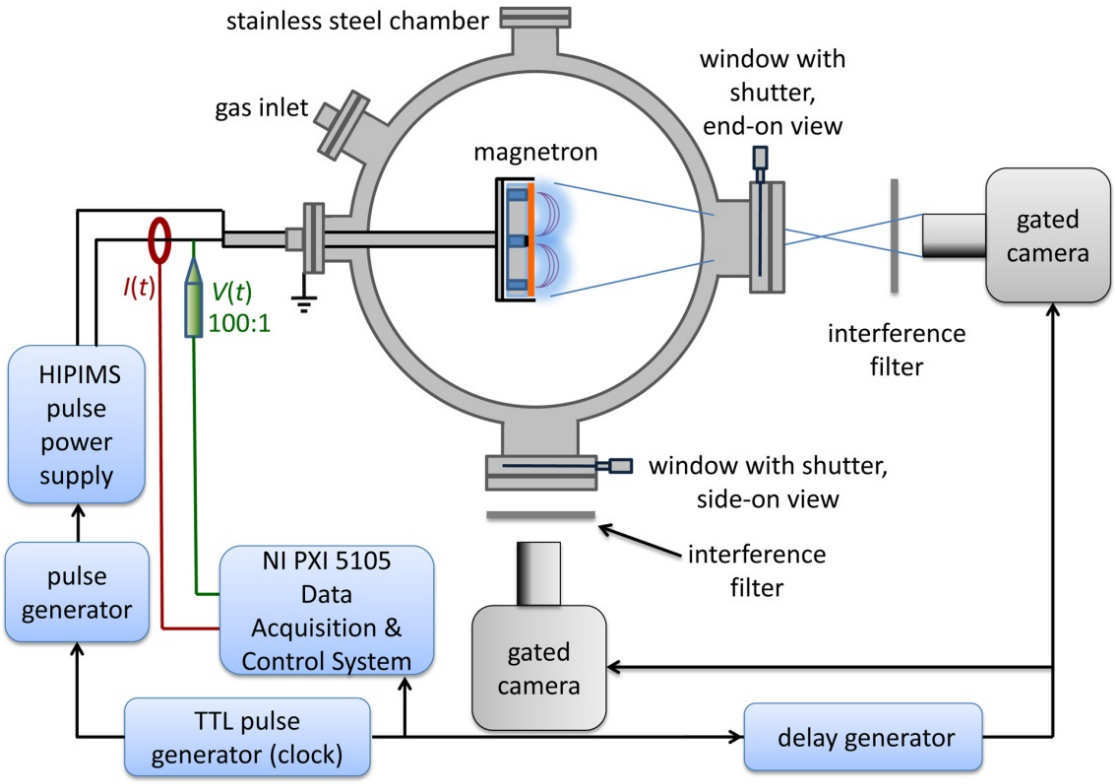

Supplementary material part 2:

Wavelength and spectroscopic information on the spectral lines used (filter data from manufacturer's specifications and spectral information from the NIST atomic data tables).

filter's nominal wave-length (nm)	filter's lower and upper wavelength (nm)	filter's trans-mission	species	wave-lengths (nm)	upper level (eV)	lower level (eV)	A_{ul} (s^{-1})	comment
394	389-399	>85%	Al I	394.40	3.1427	0.0000	4.93×10^{7}	very strong
			Al I	396.15	3.1427	0.0139	9.8×10^{7}	very strong
436	431-441	>85%	Ar II	433.12	19.6103	16.7485	5.74×10^{7}	
			Ar II	433.20	19.3054	16.4441	1.92×10^{7}	
			Ar II	433.71	24.2844	21.4265	3.4×10^{7}	
			Ar II	434.81	19.4945	16.6439	1.17×10^{8}	strong
			Ar II	435.22	19.3054	16.4574	2.12×10^{7}	
			Ar II	436.21	21.4981	18.6565	5.5×10^{6}	
			Ar II	437.08	21.4924	18.6565	6.6×10^{7}	
			Ar II	437.13	19.2611	16.4256	2.21×10^{7}	
			Ar II	437.60	19.9726	17.1400	2.5×10^{7}	
			Ar II	437.97	19.6426	16.8125	1.00×10^{8}	strong
			Ar II	438.38	19.9675	17.1400	1.1×10^{6}	
			Ar II	440.01	19.2611	16.4441	1.06×10^{7}	
			Ar II	440.10	19.2229	16.4065	3.04×10^{7}	
480	475-485	>85%	Ar II	476.486	19.8671	17.2658	6.4×10^{7}	
			Ar II	480.602	19.2229	16.6438	7.80×10^{7}	dominant
			Ar II	484.781	19.3056	16.7485	8.49×10^{7}	
630	620-640	> 90%	Al II	622.62	15.0621	13.0714	6.2×10^{7}	
			Al II	623.17	15.0621	13.0731	8.4×10^{7}	
			Al II	624.34	15.0620	13.0767	1.1×10^{8}	
			Al II	633.57	15.6058	13.6494	1.4×10^{7}	
694	689-699	>85%	Ar I	693.766	14.6936	12.9070	3.08×10^{6}	
			Ar I	696.5430	13.3278	11.5484	6.39×10^{6}	dominant
810	805-815	>50%	Ar I	810.3686	13.1532	11.6235	2.5×10^{7}	
			Ar I	811.5311	13.0757	11.5484	3.31×10^{7}	

Supplementary material part 3.
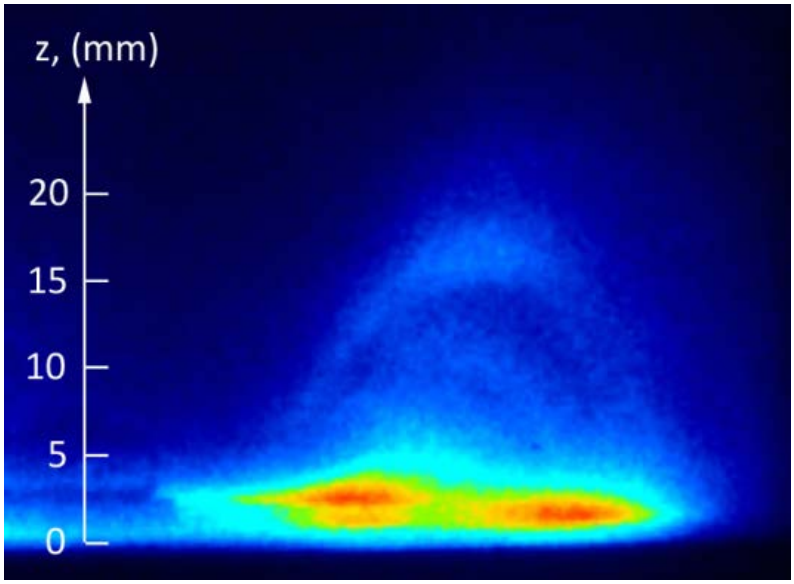
Enlarged detail of an image taken with spectrally integrated light at 100 A discharge current. Since neither atoms nor ions tend to arrange in arches, the arches seen are indicative for the role of excitation by magnetized energetic electrons.